Chemical Engineering Journal 525 (2025) 170413

Contents lists available at ScienceDirect

Chemical Engineering Journal

journal homepage: www.elsevier.com/locate/cej

Superior bridging effect of Pt NPs in all-solid-state *Z*-scheme CdS QDs/$NaTaO_3$ microcube heterojunction for highly efficient photocatalytic hydrogen evolution

Jiayi Meng, Juhua Zhang, Yamei Huang, Zizheng Wang, Yifan Liao, Quanmei Zhou, Yuchen Wei, Linlin Gao, Wei-Lin Dai *

State Key Laboratory of Porous Materials for Separation and Conversion, Shanghai Key Laboratory of Molecular Catalysis and Innovative Materials, Department of Chemistry, Fudan University, Shanghai 200438, PR China

ARTICLE INFO

Keywords:
$CdS/Pt/NaTaO_3$
Z-scheme heterojunction
Photocatalytic hydrogen evolution
Pt NPs bridging effect
$NaTaO_3$-based photocatalysts

ABSTRACT

Photocatalytic water splitting for hydrogen production is a clean and efficient way to convert solar energy into storable hydrogen fuel. Herein, a novel all-solid-state *Z*-scheme heterojunction CdS quantum dots/Pt nanoparticles/$NaTaO_3$ microcubes (CdS QDs/Pt NPs/$NaTaO_3$ MCs) was synthesized via in situ photoreduction deposition and solvothermal methods for highly efficient photocatalytic hydrogen evolution. The as-prepared $CdS/Pt/NaTaO_3$ exhibited remarkable hydrogen evolution activity of 19,844 $\mu mol \cdot g^{-1} \cdot h^{-1}$ under visible light, which is 325 times higher than that of pure $NaTaO_3$ MCs and 15 times higher than pure CdS QDs. Experimental and theoretical calculations show the strong interaction between the CdS QDs, Pt NPs, and $NaTaO_3$ MCs. Crucially, Pt NPs were strategically located at the heterojunction interface, bridging CdS QDs and $NaTaO_3$ MCs, playing a critical role as an electron mediator. Electrons efficiently transfer from $NaTaO_3$ to CdS via the Pt NPs, establishing a direct *Z*-scheme charge transfer pathway. This results in the retention of strong oxidation holes on the valence band (VB) of $NaTaO_3$ and strong reduction electrons on the conduction band (CB) of CdS, effectively promoting the separation and migration of photogenerated electron-hole pairs, and enhancing the activity of photocatalytic water splitting for hydrogen evolution. Furthermore, DFT calculations of the Gibbs free energy for hydrogen adsorption (ΔG_{H^*}) reveal that the intermediate Pt NPs in the ternary structure provide the most favorable sites for H_2 evolution, exhibiting the lowest overpotential and reaction barrier. This study provided new insights into designing stable and efficient $NaTaO_3$-based heterojunction photocatalysts.

1. Introduction

Photocatalytic water splitting for hydrogen production is widely recognized as a promising strategy to address global energy crises and environmental degradation [1–4]. Currently, the focus and hotspot of research in the field of photocatalysis is the design and development of highly efficient photocatalysts. Among the many developed photocatalytic materials [5–7], sodium tantalate ($NaTaO_3$) has attracted much attention because of its excellent catalytic activity in photocatalysis [8,9]. The main reason is that the conduction band (CB) formed by Ta 5d orbitals in $NaTaO_3$ has a more negative potential. At the same time, the unique [TaO_6] octahedral orientation of $NaTaO_3$ enables the efficient separation of photogenerated carriers. As a widely used tantalate semiconductor material, $NaTaO_3$ has excellent photocatalytic activity in the ultraviolet (UV) region, outstanding chemical stability, and environmental friendliness, making it highly promising for applications in the photocatalytic field [10–13]. However, the wide band gap and the high combination rate of photogenerated carriers of $NaTaO_3$ limit its photocatalytic hydrogen production performance. In order to overcome the above problems, researchers have used non-metallic doping, surface noble metal loading, and compounding with semiconductors to modify the surface of $NaTaO_3$ to obtain composite catalysts with excellent catalytic activity to improve the separation efficiency of the carriers [14–16]. However, applications in photocatalytic water splitting for H_2 production have to be further developed. Therefore, the design and development of a new $NaTaO_3$-based composite catalyst responsive to visible light for the photocatalytic decomposition of water to produce hydrogen has aroused great interest and concern among researchers.

* Corresponding author.
E-mail address: wldai@fudan.edu.cn (W.-L. Dai).

https://doi.org/10.1016/j.cej.2025.170413
Received 8 September 2025; Received in revised form 27 October 2025; Accepted 1 November 2025
Available online 3 November 2025

It is well known that cadmium sulfide (CdS), as a typical II-VI semiconductor, is characterized by its controllable morphology and suitable structure of energy band [17–21]. However, the strong photocorrosion problem of CdS greatly shortens its service life as a photocatalyst, which hinders its practical application in photocatalysis. In addition, the photogenerated carriers of single CdS materials are easily recombined on their surfaces, and thus the hydrogen production activity of CdS is still low. Considering these research bottlenecks, several attempts have been explored to enhance the overall photocatalytic performance of CdS materials, including morphology modification, elemental doping, co-catalyst loading, and heterojunctions with other semiconductor materials. Among them, modifying the morphology and structure of CdS into quantum dots (QDs) by changing the synthesis method and conditions can provide unique optical and electronic properties, promote intermolecular interactions, and accelerate charge transfer by taking advantage of the quantum confinement effect and surface effect of CdS QDs. Therefore, the composites modified with CdS QDs are expected to be new high-efficiency hydrogen evolution photocatalysts with visible light response [22,23].

In recent years, the construction of all-solid-state *Z*-scheme heterojunctions by compositing two different semiconductors and a suitable solid-state electronic medium has been regarded as one of the most effective photocatalytic systems [24–28]. The nature of this intermediate electronic medium and the interfacial bonding ability directly determine the performance of the all-solid-state *Z*-scheme heterojunction. Currently, the most widely used electron mediators are still noble metals, such as Pt, Au, Ag nanoparticles (NPs), etc. The all-solid-state *Z*-scheme heterojunction system can increase the interfacial contact between semiconductors and improve the overall catalytic stability and light absorption [29–32]. Furthermore, the all-solid-state nature of the *Z*-scheme heterojunction offers distinct advantages over conventional liquid-phase Z-scheme systems, which typically rely on soluble redox mediators (e.g., I_3^-/I^- or Fe^{3+}/Fe^{2+}). The solid-state electron mediator (Pt NPs) not only facilitates efficient directional electron transfer but also enhances the structural integrity and operational stability of the photocatalyst by avoiding issues such as photocorrosion of CdS, reverse reactions, and the diffusion limitations associated with liquid redox couples. The most significant advantage is that the separation efficiency of photogenerated electrons and holes in the composite catalysts has been greatly improved, and the redox sites can be completely separated.

In this work, all-solid *Z*-scheme heterojunction CdS/Pt/$NaTaO_3$ microcubic composites were synthesized by photoreduction deposition and solvothermal methods, and their photocatalytic decomposition of water for hydrogen production was investigated. By adjusting the loading quality of Pt NPs and CdS QDs, it is found that the 25 %CdS/2 % Pt/$NaTaO_3$ has the largest photocatalytic hydrogen evolution value up to 19.8 $mmol{\cdot}g^{-1}{\cdot}h^{-1}$ under visible light. Based on the results of different characterizations and DFT theoretical calculations, the structure of *Z*-scheme heterojunction with Pt NPs tightly coupled as a bridge is proposed, which promotes the effective separation of photogenerated electrons and holes, thereby enhancing the hydrogen production efficiency.

2. Experimental

2.1. Preparation of $NaTaO_3$

$NaTaO_3$ MCs were synthesized by hydrothermal precipitation. The preparation process was as follows: 0.75 M NaOH solution was dissolved in water (80 mL) and stirred magnetically for 10 min, then 0.884 g of tantalum pentoxide (Ta_2O_5) was added, and stirred for 30 min. The mixture was transferred to a 100 mL of Teflon-lined reactor and kept at 180 °C for 24 h. The mixture was then filtered, washed several times with large amounts of deionized water and ethanol, and dried at 100 °C overnight.

2.2. Preparation of Pt/$NaTaO_3$

Pt/$NaTaO_3$ was prepared by photoreduction deposition. 0.30 g of the prepared $NaTaO_3$ was dispersed into a 100 mL of beaker containing 50 mL of deionized water and ultrasonicated for 30 min, then transferred to a photoreactor, and 10 mL of methanol and 1.6 mL of 10 mg/mL $H_2PtCl_6{\cdot}6H_2O$ solution were added. The reaction temperature was controlled at 25 °C, and the process was irradiated by a 300 W xenon lamp without a cut-off wavelength for 3 h with magnetic stirring. The precipitate was then filtered, washed with large amounts of deionized water and ethanol, and finally dried in a vacuum oven at 80 °C overnight. The $NaTaO_3$ MCs with different loadings of Pt NPs were obtained by varying the volume of $H_2PtCl_6{\cdot}6H_2O$ aqueous solution added dropwise, and were recorded as 0.5 %Pt/$NaTaO_3$, 1 %Pt/$NaTaO_3$, 2 %Pt/$NaTaO_3$, 3 %Pt/$NaTaO_3$, and 5 % Pt/$NaTaO_3$, respectively.

2.3. Preparation of CdS/Pt/$NaTaO_3$, CdS QDs, and CdS/$NaTaO_3$

Further, *Z*-scheme heterojunction CdS/Pt/$NaTaO_3$ was successfully synthesized by the solvothermal method. The detailed procedure was as follows: firstly, 200 mg of the prepared Pt/$NaTaO_3$ binary composites and different masses of $Cd(CH_3COO)_2{\cdot}2H_2O$ were added into a 100 mL beaker with 50 mL of DMSO and dispersed by ultrasonication for 1 h, and then magnetically stirred at a medium speed for 1 h. The reaction suspension was then transferred into a 100 mL of PTFE-lined hydrothermal kettle and reacted at 180 °C for 12 h to produce a yellow precipitate. Then the suspension was transferred to a 100 mL Teflon-lined reactor and reacted at 180 °C for 12 h to produce a yellow precipitate. Centrifuge the yellow precipitate and wash it three times with deionized water and ethanol, respectively. Then vacuum dry it overnight at 80 °C to obtain CdS/Pt/$NaTaO_3$. The 2 %Pt/$NaTaO_3$ composites modified with different masses of CdS QDs were marked as 10 %CdS/2 %Pt/$NaTaO_3$, 15 %CdS/2 %Pt/$NaTaO_3$, 25 %CdS/2 %Pt/$NaTaO_3$, and 40 % CdS/2 %Pt/$NaTaO_3$, respectively. The preparation of pure-phase CdS QDs and binary CdS/$NaTaO_3$ composite catalysts was similar, except that no Pt/$NaTaO_3$ MCs and no Pt NPs were added.

3. Results and discussion

3.1. Materials synthesis and characterization

Fig. 1 briefly illustrates the preparation process of CdS/Pt/$NaTaO_3$ composite catalysts. Firstly, the $NaTaO_3$ microcubic structure was obtained by a simple hydrothermal method to provide support for further loading of Pt NPs and CdS QDs. Pt NPs were then loaded onto the $NaTaO_3$ surface via an in situ photoreduction deposition method, followed by the solvothermal growth of CdS QDs to form the final ternary composite. A binary CdS/$NaTaO_3$ counterpart was also prepared without Pt NPs for comparative purposes. The choice of in situ photoreduction for Pt deposition is critical. Unlike conventional methods such as impregnation reduction, this technique utilizes the photogenerated electrons from $NaTaO_3$ to directly reduce Pt precursors at the semiconductor surface. This mechanism ensures a more uniform distribution of Pt NPs and fosters a stronger metal-support interaction, both of which are crucial for facilitating interfacial charge transfer and stabilizing the catalyst structure.

Scanning electron microscopy (SEM), transmission electron microscopy (TEM), and high-resolution transmission electron microscopy (HRTEM) analyses reveal the morphological and structural characteristics of the synthesized materials. As shown in Fig. 2a and Fig. S1, solvothermally synthesized CdS QDs exhibit an average size of 5.81 nm but suffer from significant agglomeration due to their high surface energy. This disordered arrangement promotes rapid recombination of photogenerated charge carriers. In contrast, $NaTaO_3$ (Fig. 2b, Fig. S2) displays well-defined MCs with smooth surfaces. For Pt/$NaTaO_3$, deposited Pt NPs are uniformly dispersed on the surface of $NaTaO_3$ MCs

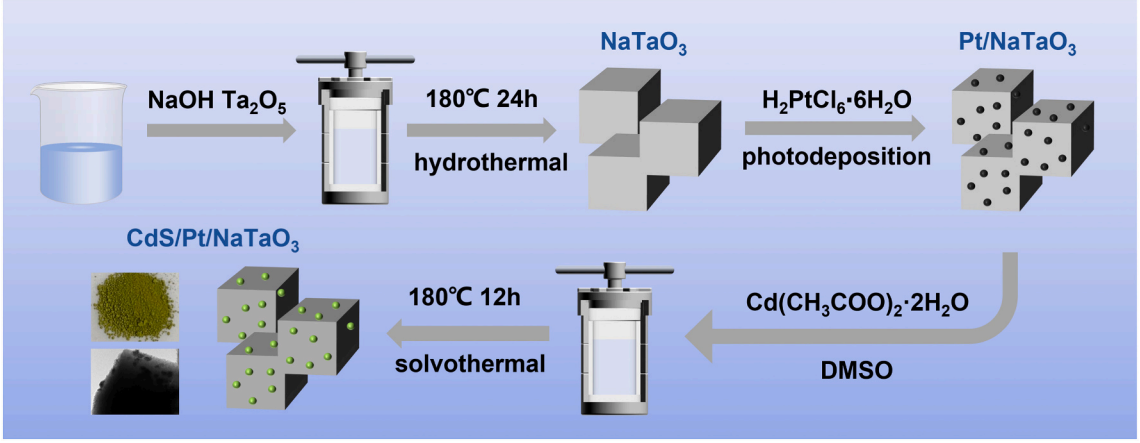

Fig. 1. Preparation process of the CdS/Pt/$NaTaO_3$ MCs by the photodeposition and hydrothermal method.

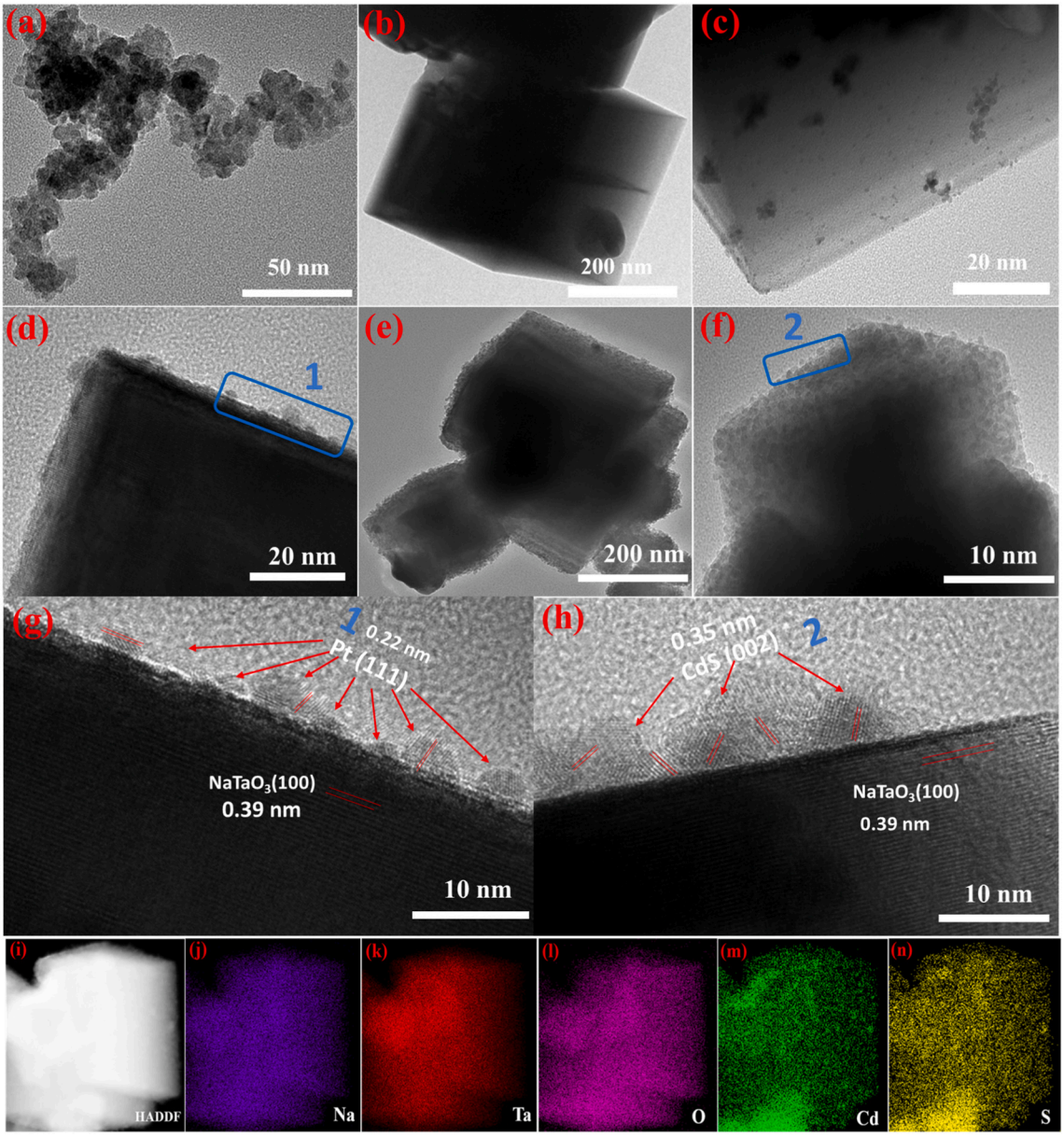

Fig. 2. TEM images of (a) CdS, (b) $NaTaO_3$, (c,d) 2 %Pt/$NaTaO_3$, and (e,f) 25 %CdS/$NaTaO_3$; HRTEM images of (g) 2 %Pt/$NaTaO_3$ and (h) 25 %CdS/$NaTaO_3$; (i-n) the corresponding EDX mapping profiles of 25 %CdS/$NaTaO_3$.

via photodeposition (Fig. 2c-d). Concurrently, partial agglomeration of Pt NPs on the $NaTaO_3$ microcube surfaces was observed, attributable to the relatively high Pt loading (2 wt%). For the CdS/$NaTaO_3$ binary composite (Fig. 2e-f), CdS QDs achieve uniform surface coverage on $NaTaO_3$ MCs. Critically, Fig. 2g–h reveals intimate interfacial contact between Pt NPs and $NaTaO_3$ MCs, as well as those between CdS QDs and $NaTaO_3$. The observed lattice spacings of 0.22, 0.35, and 0.39 nm are attributed to the (111) plane of the Pt NPs, the (002) plane of the CdS QDs [33,34], and the (100) plane of $NaTaO_3$ [35,36], respectively. Elemental mapping (Fig. 2i-n) further verifies the uniform distribution of Na, Ta, O, Cd, and S throughout the CdS/$NaTaO_3$ composite, confirming successful heterojunction formation.

In Fig. 3a-c, $NaTaO_3$ maintains the characteristic microcube-like structure in the CdS/Pt/$NaTaO_3$ system. The solvothermal synthesis achieved dual-anchoring of CdS QDs on $NaTaO_3$ MCs through Pt NPs interfacial mediation, with CdS QDs partially immobilized on Pt-decorated surfaces and partially on bare $NaTaO_3$ substrates. Meanwhile, the size of CdS QDs grown in situ in the CdS/Pt/$NaTaO_3$ system is close to that of pure-phase CdS QDs as well as binary CdS/$NaTaO_3$, which suggests that the formation of the ternary CdS/Pt/$NaTaO_3$ composite structure does not affect the structure and morphology of CdS QDs. In Fig. 3d-e, Pt NPs are loaded on $NaTaO_3$ and located at the heterojunction interface between $NaTaO_3$ and CdS QDs, acting like a bridge to connect $NaTaO_3$ and CdS QDs. The parts marked by orange are CdS QDs, and the lattice stripe with a lattice spacing of 0.35 nm is attributed to the (002) crystal plane of CdS QDs. The parts marked by red circles are Pt NPs, and the lattice stripes of 0.23 nm and 0.39 nm correspond to the (111) and (100) crystal planes of Pt NPs and $NaTaO_3$, respectively. Based on the different lattices of the TEM images of Pt NPs and CdS QDs, it can be observed that the CdS QDs completely cover the Pt NPs. The elemental mapping of the ternary composite heterojunction (Fig. 3f-m) confirmed the presence of six elements, Na, Ta, O, Cd, S, and Pt, and further verified the successful preparation of the CdS/Pt/$NaTaO_3$ system.

The bulk crystalline phase composition of the CdS/Pt/$NaTaO_3$ system was analyzed using X-ray diffraction (XRD) (Fig. 4a, Fig. S3). For the

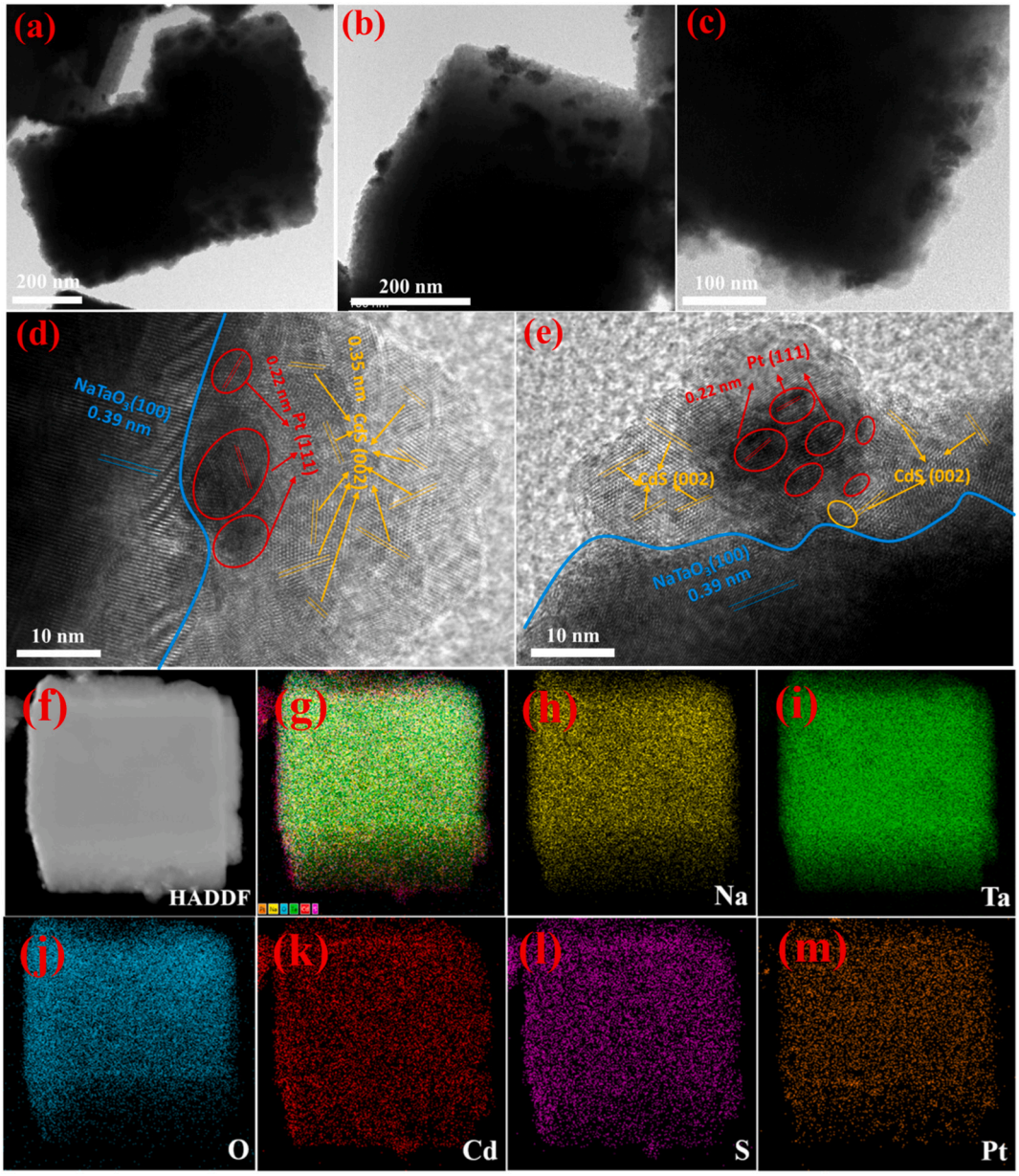

Fig. 3. TEM images of (a-c) 25 %CdS/2 %Pt/$NaTaO_3$; (d-e) HRTEM images of 25 %CdS/2 %Pt/$NaTaO_3$; (f-m) the corresponding EDX mapping profiles of 25 %CdS/2 %Pt/$NaTaO_3$.

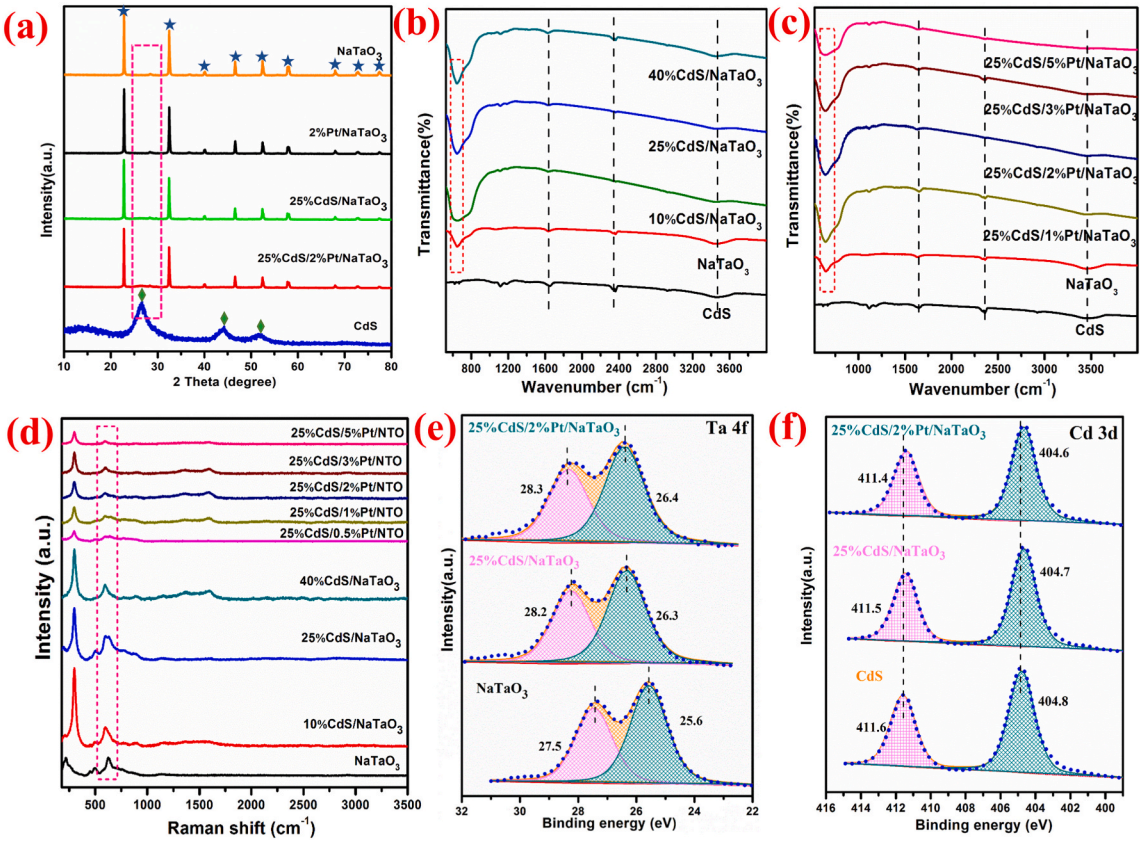

Fig. 4. (a) XRD spectra of the as-fabricated catalysts; (b, c) FT-IR spectra of various catalysts in CdS/Pt/$NaTaO_3$ system; (d) Raman spectra of the different samples in CdS/Pt/$NaTaO_3$ system; XPS spectra of $NaTaO_3$, CdS, CdS/$NaTaO_3$ and CdS/Pt/$NaTaO_3$: (e) Ta 4f, (f) Cd 3d.

pure-phase $NaTaO_3$ MCs sample, nine diffraction peaks with XRD 2θ values of 22.8°, 32.5°, 40.1°, 46.6°, 52.4°, 57.8°, 68.0°, 72.8°, and 77.4° can be attributed to the monoclinic crystal system $NaTaO_3$, with (100), (110), (−111), (200), (210), (−211), (220), (−212), and (310) (JCPDS No. 74–2481), respectively, indicating the successful synthesis and high crystallinity of $NaTaO_3$ MCs [37]. In the XRD pattern of pure-phase CdS QDs, three characteristic diffraction peaks appearing at 26.6°, 43.8°, and 52.0° are attributed to the (002), (110), and (112) crystal planes of hexagonal crystalline phase CdS (JCPDS NO. 41–1049), respectively. The absence of impurity peaks in the XRD spectra of both pure $NaTaO_3$ and CdS indicates that pure monoclinic $NaTaO_3$ and hexagonal CdS were synthesized [38,39]. In addition, the characteristic diffraction patterns of Pt NPs were not observed in the XRD pattern of Pt/$NaTaO_3$, which was caused by the lower loading concentration of Pt and the smaller particle size of Pt NPs [40,41]. As for the absence of the characteristic diffraction patterns of Pt NPs (also detected in the CdS/Pt/$NaTaO_3$ composite catalysts), in addition to the presence of the two influencing factors mentioned above, another important reason is that the Pt NPs are completely encapsulated by the CdS QDs, which leads to the further reduction of their particle size. Fourier-transform infrared (FT-IR) spectra were used to verify the successful preparation of the samples (Fig. 4b-c). All catalysts except CdS show strong peaks around 600 cm^{-1}, which are attributed to the characteristic telescopic vibrational peaks of Ta—O and correlate with the stretching model of [TaO_6] octahedra. The peak at 1660 cm^{-1} is attributed to the H-O-H stretching vibration of water molecules bonded to Na^+. The large and broad peaks at 3000–3500 cm^{-1} can be ascribed to the O—H stretching vibration of H_2O adsorbed on the catalyst surface. The strong peak at 600 cm^{-1} in the Raman spectrum is attributed to the telescopic vibrational peak of Ta—O in the angularly linked [TaO_6] octahedra (Fig. 4d and Fig. S4) [42]. The surface elemental composition and chemical state of the CdS/Pt/$NaTaO_3$ catalyst were further analyzed using X-ray photoelectron spectroscopy (XPS). The XPS survey spectrum of the CdS/Pt/$NaTaO_3$ system (Fig. S5) clearly shows the presence of the characteristic peaks of each element in the as-prepared catalysts. Table S1 presents the surface elemental compositions of the prepared catalysts. Significantly reduced Na and Ta surface concentrations in CdS/$NaTaO_3$ and CdS/Pt/$NaTaO_3$ relative to pristine $NaTaO_3$ indicate near-complete encapsulation of $NaTaO_3$ MCs by CdS QDs. Concurrently, the lower Pt surface content (0.5 %) detected by XPS in CdS/Pt/$NaTaO_3$ compared with Pt/$NaTaO_3$ (1.4 %) confirms extensive coverage of Pt NPs by CdS QDs, highlighting the bridging role of Pt NPs (Table S2). These findings strongly corroborate TEM and XRD characterization result. As shown in Fig. 4e, the two peaks appearing around 27.5 eV and 25.6 eV are attributed to Ta $4f_{5/2}$ and Ta $4f_{7/2}$, respectively, which is consistent with the chemical state (+5) valence [10,11]. After complexation with Pt NPs and CdS QDs, the Ta 4f binding energies of the binary 25 %CdS/$NaTaO_3$ and ternary 25 % CdS/Pt/$NaTaO_3$ complexes are shifted to higher positions at 28.2, 26.3 eV, and 28.3, 26.4 eV, respectively, suggesting that strong interactions between $NaTaO_3$, Pt, and CdS lead to electron transfer. In Fig. 4f, it can be observed that the binding energies of Cd $3d_{3/2}$ and Cd $3d_{5/2}$ of pure-phase CdS are located at 411.6 eV and 404.8 eV. After the formation of ternary CdS/Pt/$NaTaO_3$ composites, the Cd 3d peak positions were shifted to the low binding energies by 0.2 eV, which further confirmed the existence of strong interactions among $NaTaO_3$, Pt NPs, and CdS QDs, indicating the higher electron density of CdS in the ternary composite. Electrons tend to be transferred from $NaTaO_3$ to CdS when three-phase CdS/Pt/$NaTaO_3$ heterojunctions are formed.

3.2. *Photocatalytic property*

To systematically evaluate the photocatalytic activity of the CdS/Pt/

$NaTaO_3$ system, photocatalytic hydrogen evolution activity experiments were carried out under visible light irradiation. In Fig. 5a-c, the hydrogen production activity of pure-phase CdS QDs was 1331 $\mu mol \cdot g^{-1} \cdot h^{-1}$ while that of pure-phase $NaTaO_3$ was only 60.5 $\mu mol \cdot g^{-1} \cdot h^{-1}$ when lactic acid was used as the sacrificial agent. Although CdS/$NaTaO_3$ exhibits lower photocatalytic hydrogen evolution activity than pristine CdS after CdS QDs loading, the 25 % mass fraction CdS loading achieves peak performance (1058.8 $\mu mol \cdot g^{-1} \cdot h^{-1}$). The inferior activity of the Pt/CdS binary composite, compared to pure CdS, stems from the conventional role of Pt as an electron sink. This forms a Schottky junction that, without efficient hole consumption, exacerbates CdS photocorrosion and may block active sites. This result underscores that in our ternary system, Pt functions uniquely as a *Z*-scheme electron mediator rather than a traditional co-catalyst. When loading Pt NPs between CdS QDs and $NaTaO_3$ MCs, a series of CdS/Pt/$NaTaO_3$ ternary composite catalysts could be formed. 25 %CdS/2 %Pt/$NaTaO_3$ could reach 19,844 $\mu mol \cdot g^{-1} \cdot h^{-1}$, which was 325 times higher than that of $NaTaO_3$ MCs and 15 times higher than that of CdS QDs, respectively. 25 %CdS/2 %Pt/$NaTaO_3$ demonstrates exceptional photocatalytic H_2 evolution, surpassing many previously reported Z-scheme photocatalysts (Fig. S6, Table S3). At the 2 % loading, the deposited Pt nanoparticles reach a density that effectively bridges the CdS QDs and $NaTaO_3$ MCs, thereby facilitating efficient Z-scheme electron transfer without significantly blocking active sites. However, when the Pt loading exceeds 2 %, this agglomeration becomes more pronounced, leading to a reduction in the number of available active sites and interfacial contact area, which ultimately impairs the overall performance. The hydrogen production performance of all CdS/Pt/$NaTaO_3$ composite photocatalysts was substantially improved compared with CdS/$NaTaO_3$, Pt/$NaTaO_3$, and Pt/CdS. This finding demonstrates that the synthesized all-solid-state heterojunction structure with Pt NPs as a bridge significantly enhances the photocatalytic activity. Besides, lactic acid was determined as the optimal sacrificial agent for this reaction system (Fig. 5d). The best catalyst mass is 100 mg (Fig. 5e). In addition, the 25 %CdS/2 %Pt/$NaTaO_3$ MCs had the best apparent quantum efficiency (AQE, 7.9 %) at 350 nm (Fig. 5f). In Fig. 5g, there was no significant deactivation of the catalyst after five photocatalytic cycles, and its activity still exceeded 90 % of the initial 4 h average hydrogen production. Meanwhile, the TEM images (Fig. S7) of the catalysts before and after the cycling photoreaction showed that the structure of the all-solid 25 %CdS/2 %Pt/$NaTaO_3$ heterojunction did not undergo any obvious changes, and these results consistently demonstrated that this system had excellent structural stability. This catalyst mitigates the photocorrosion of CdS to a certain extent. The *Z*-scheme heterojunction and Pt bridging enable the highly reactive photogenerated holes (h^+) on the CdS valence band to be rapidly consumed through recombination with electrons (e^-) from $NaTaO_3$ via the Pt bridge, thereby fundamentally suppressing the photocorrosion reaction pathway.

3.3. Optical, photoelectric, and electrical properties

To illustrate the correlation between the structure of CdS/Pt/$NaTaO_3$ heterojunctions and their enhanced photocatalytic activity, a comprehensive series of tests was performed. In Fig. 6a, the photoluminescence (PL) spectral intensity of 25 %CdS/2 %Pt/$NaTaO_3$ composite catalysts is significantly reduced compared with the single $NaTaO_3$ and CdS/$NaTaO_3$, which indicates that the loading of CdS QDs and the introduction of Pt NPs can effectively suppress the combination of photogenerated carriers and enhance the separation of photogenerated carriers in the CdS/Pt/$NaTaO_3$. In Fig. 6b, the photocurrent response intensity of 25 %CdS/2 %Pt/$NaTaO_3$ is superior to that of $NaTaO_3$ and 25 %CdS/$NaTaO_3$, which indicates that the photogenerated electrons and holes are efficiently separated and transferred in the CdS/Pt/$NaTaO_3$ heterojunction. As shown in Fig. 6c, 25 %CdS/2 %Pt/$NaTaO_3$ has the smallest radius compared to $NaTaO_3$ and 25 %CdS/$NaTaO_3$, which implies that it has the lowest resistance and higher charge carrier transport efficiency.

The ultraviolet-visible diffuse reflectance spectroscopy (UV–Vis DRS) shows that the $NaTaO_3$ MCs exhibit high absorption properties in the UV region, with the absorption band located around 315 nm (Fig. S8, Fig. S9). When composited with CdS QDs, the absorption edge of CdS/$NaTaO_3$ is significantly red-shifted, and a new optical absorption band appears at near 530 nm. When the CdS/Pt/$NaTaO_3$ ternary complexes were further formed, the electronic coupling at the interface between the Pt NPs and the CdS QDs led to a significant enhancement of the absorption in the visible region in the 600–800 nm range. The color of each sample is shifted in the same direction as the absorption edge of the UV–Vis DRS (Fig. S10). Based on the previous UV–Vis DRS results, the

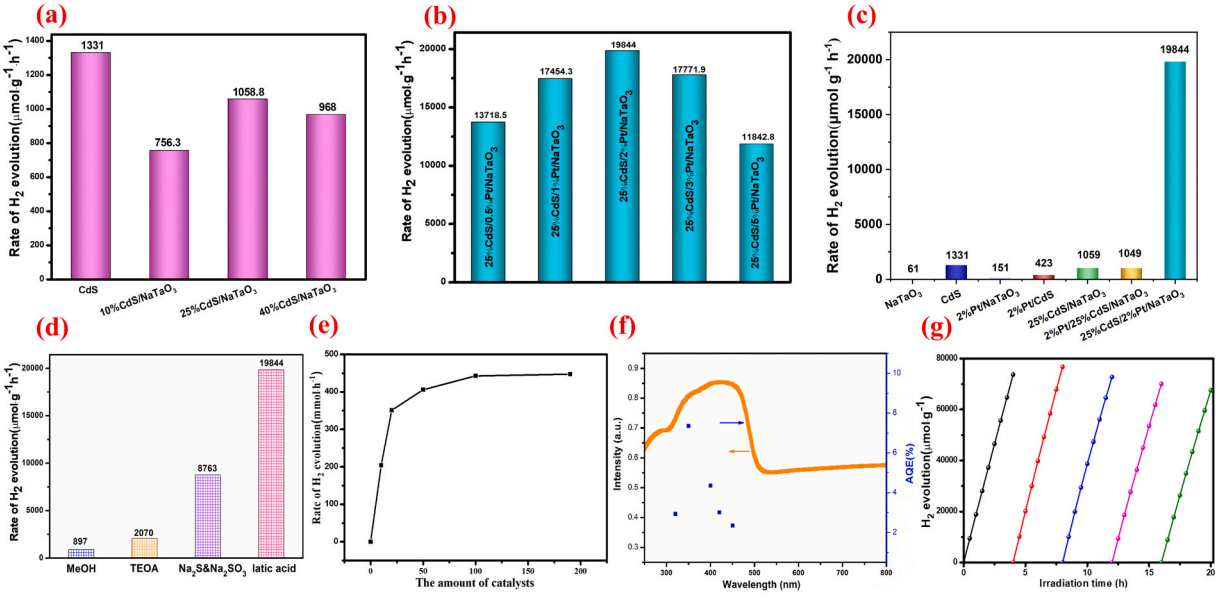

Fig. 5. (a) H_2 evolution rate of as-prepared catalysts in CdS/$NaTaO_3$ system; (b) H_2 evolution rate of different CdS/Pt/$NaTaO_3$; (c) H_2 evolution rate of as-prepared catalysts in CdS/Pt/$NaTaO_3$ system; (d) Hydrogen evolution rate of 25 %CdS/2 %Pt/$NaTaO_3$ using different sacrificial agents; (e) Quality-dependent curves of photocatalytic hydrogen evolution over 25 %CdS/2 %Pt/$NaTaO_3$; (f) Apparent quantum efficiency over 25 %CdS/2 %Pt/$NaTaO_3$; (g) Recycling stability test of 25 % CdS/2 %Pt/$NaTaO_3$.

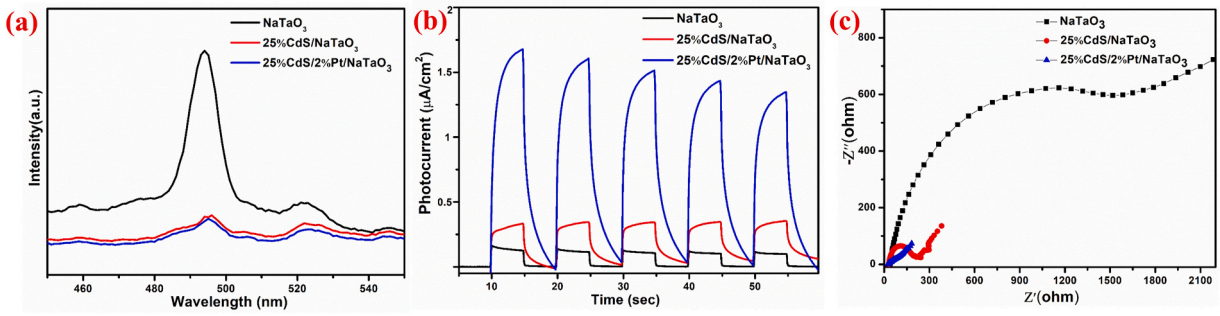

Fig. 6. (a) PL spectrum; (b) Transient photocurrent responses; and (c) EIS Nyquist plots of $NaTaO_3$, 25 %CdS/$NaTaO_3$, 25 %CdS/2 %Pt/$NaTaO_3$.

energy band gaps (E_g) of $NaTaO_3$ and CdS QDs were 3.85 eV and 2.20 eV, respectively, using the Kubelka-Munk transformation with $(ah\nu)^{1/2}$ versus ($h\nu$) mapping (Fig. 7a). Meanwhile, the Mott-Schottky curve was further used to determine the flat band potentials (E_{fb}) of the CdS and $NaTaO_3$ as −0.90 V and − 0.54 V, respectively, using the saturated calomel electrode (SCE) as a reference (Fig. 7b-c). In general, the voltage of the reference electrode differs from that of the standard hydrogen electrode by approximately 0.2 V. Considering that the CB value of n-type semiconductors is typically 0.2 eV lower than the flat-band potential, it can be inferred that the accurate CB positions of $NaTaO_3$ and CdS are approximately −0.54 eV and − 0.90 eV, respectively. The value satisfies the potential requirements for photocatalytic hydrogen production, indicating it is thermodynamically feasible. Based on the E_g and CB position, the valence band (VB) of $NaTaO_3$ and CdS are derived as 3.31 eV and 1.30 eV. As shown in Fig. 7d, the energy band structure formed between $NaTaO_3$ and CdS is a staggered type.

3.4. Theoretical calculation and photocatalytic mechanism

In order to gain a deeper understanding of the electron-hole transport pathways, we conducted theoretical calculations using density functional theory (DFT) and the GGA-PBE formula for $NaTaO_3$, binary CdS/$NaTaO_3$, and ternary CdS/Pt/$NaTaO_3$ composite materials, respectively. Fig. 8a-c presents the structural models of $NaTaO_3$, CdS/$NaTaO_3$, and CdS/Pt/$NaTaO_3$. Fig. 8d-i illustrate the optimized calculations of the local and total density of states (DOS) and the electronic band structures of the systems. The partial density of states distribution of CdS/Pt/$NaTaO_3$ reveals a higher electron density at the Fermi level compared to $NaTaO_3$ and CdS/$NaTaO_3$, which is more conducive to photocatalytic hydrogen evolution (Fig. 8d-f). The curve of CdS/Pt/$NaTaO_3$ at the CB minimum (CBM) is smoother than those of pure $NaTaO_3$ and binary CdS/$NaTaO_3$, indicating improved charge separation efficiency in the composite CdS/Pt/$NaTaO_3$ (Fig. 8g-i). Moreover, a significant increase in atomic orbital hybridization is observed in CdS/Pt/$NaTaO_3$ compared to single-phase $NaTaO_3$ and binary CdS/$NaTaO_3$. This dense electronic band structure is more favorable for electron

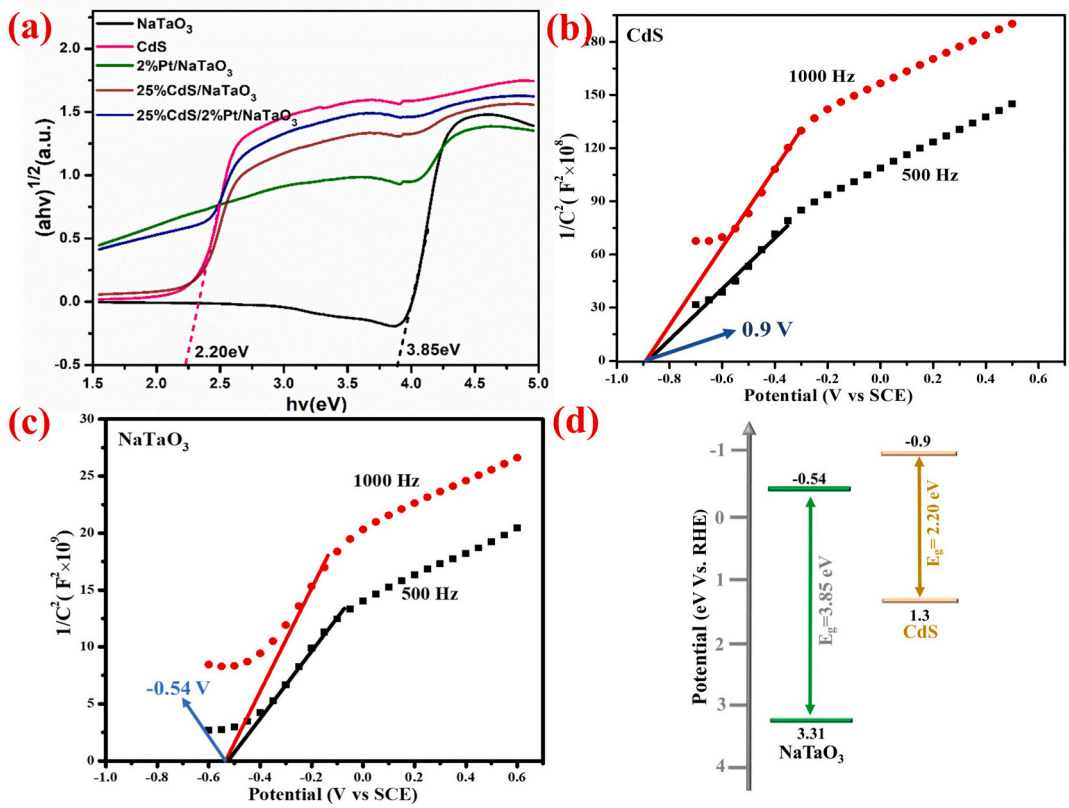

Fig. 7. (a) Tauc plots of different samples; Mott-Schottky plots of (b) CdS and (c) $NaTaO_3$; (d) Schematic illustration of band structures of $NaTaO_3$ and CdS.

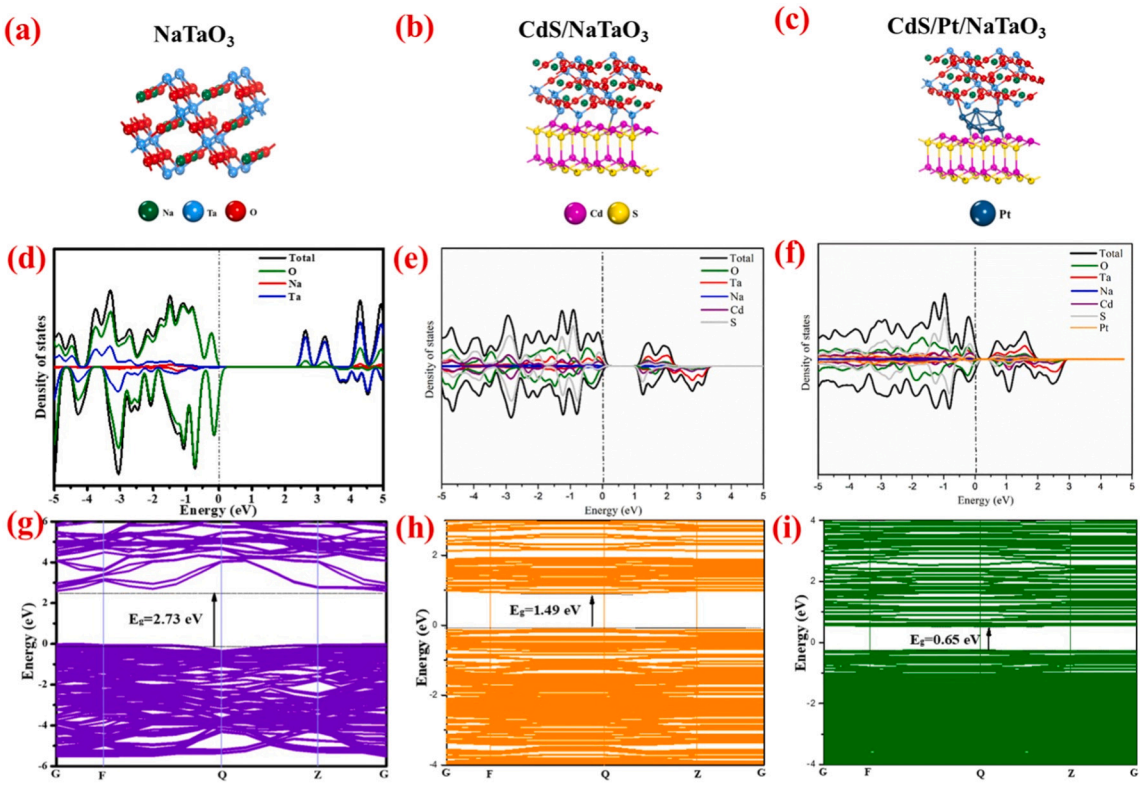

Fig. 8. (a-c) Schematic structure models; (d-f) The local and total density of states; (g-i) Electron energy band structure of $NaTaO_3$, $CdS/NaTaO_3$, and $CdS/Pt/NaTaO_3$ heterostructure.

transfer during photocatalytic hydrogen production.

In addition, by computationally simulating the interface of the $CdS/Pt/NaTaO_3$ heterojunction complex, the differential charge density distribution at the interface can be visualized (Fig. 9a-c). The electrons (highlighted red region) are concentrated on the CdS side, and the electron-deficient region (yellow region) is concentrated on the $NaTaO_3$ side, where Pt acts as a conductor and the electrons are transferred from $NaTaO_3$ through Pt to the CdS structure. This is consistent with the electron transfer path discussed in the previous XPS analysis part. This result further illustrates the significant bridging role of Pt NPs in $CdS/Pt/NaTaO_3$ composites and the role of the all-solid heterojunction structure in facilitating the directional transfer of electrons.

Electron paramagnetic resonance (EPR) spectroscopy was further used to investigate specific charge transfer mechanisms. DMPO was used as a spin label to detect superoxide radical ($\cdot O_2^-$) and hydroxyl radical ($\cdot OH$) signals in methanol solution. As shown in the Fig. S11 and Fig. S12, no $\cdot O_2^-$ signal was detected under dark conditions. However, under illumination, $CdS/Pt/NaTaO_3$ exhibits a significantly stronger $\cdot O_2^-$ and $\cdot OH$ signals than $NaTaO_3$ and CdS. This suggests that more $\cdot O_2^-$ and $\cdot OH$ radicals are generated in the $CdS/Pt/NaTaO_3$ composite material. Since $\cdot O_2^-$ is produced by the reduction of photogenerated electrons and $\cdot OH$ are produced by the oxidation of photogenerated holes, the higher signal intensity of $CdS/Pt/NaTaO_3$ indicates stronger charge carrier separation capability. The above analysis indicates that faster charge migration and more effective charge separation in $CdS/Pt/NaTaO_3$ are the key drivers for its exceptional activity of photocatalytic hydrogen evolution.

The hydrogen atom adsorption sites on $NaTaO_3$, $CdS/NaTaO_3$, and $CdS/Pt/NaTaO_3$ were shown in Fig. 10a-b. The Gibbs adsorption free energy of H atoms (ΔG_{H^*}) of single $NaTaO_3$ and binary $CdS/NaTaO_3$ heterojunctions are −0.4916 eV and − 0.3573 eV, respectively, and the ΔG_{H^*} of $CdS/Pt/NaTaO_3$ is greatly reduced to −0.1636 eV, which is close to zero. This result indicates that the ternary $CdS/Pt/NaTaO_3$ heterojunction formed by intermediate-loaded Pt NPs has a lower overpotential in the process of splitting water into hydrogen, which is more favorable for hydrogen generation. The Pt NPs exhibit outstanding

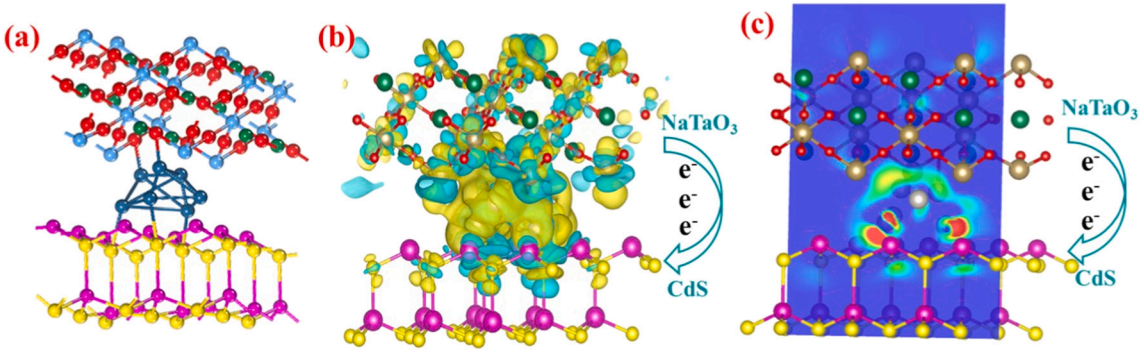

Fig. 9. (a,b) Electron density distribution at the $CdS/Pt/NaTaO_3$ interface; (c) 2D map of interfacial electron distribution.

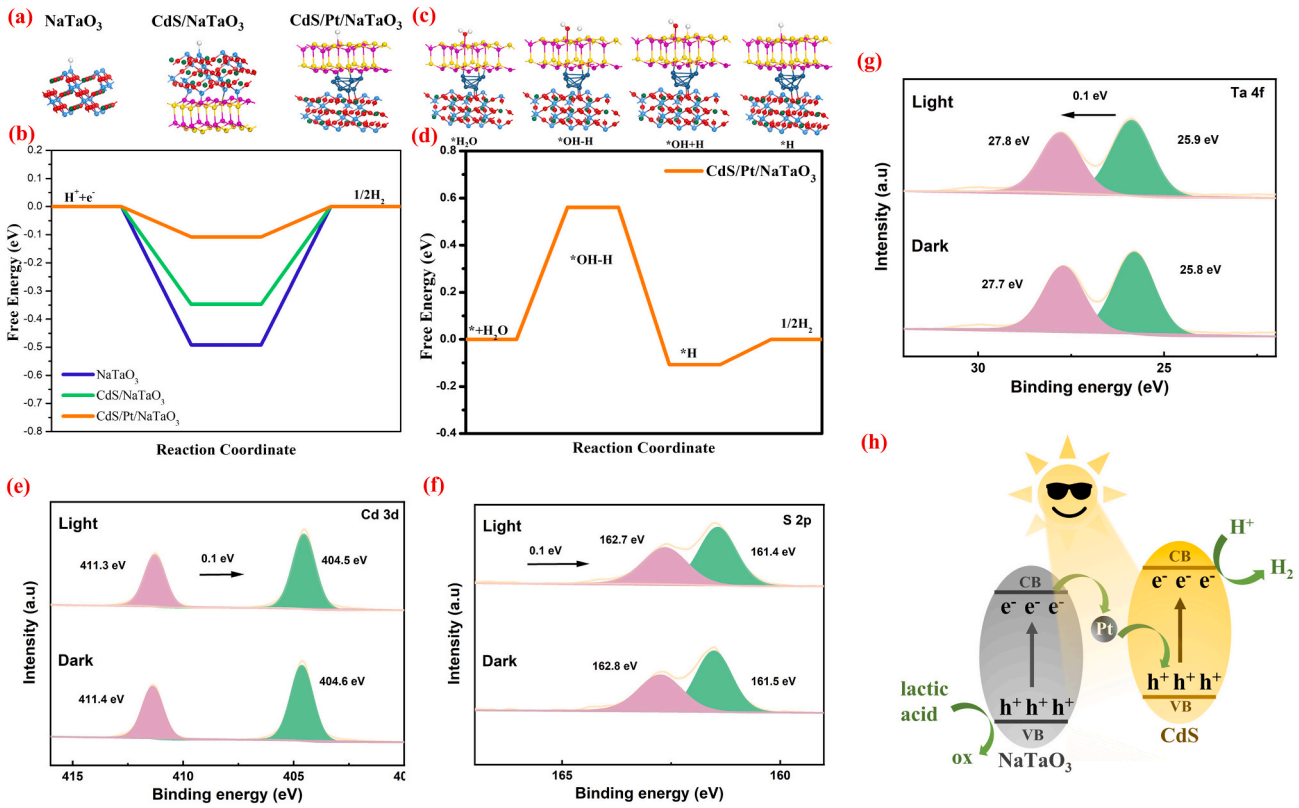

Fig. 10. (a) Atomic structures of hydrogen adsorption sites on $NaTaO_3$, $CdS/NaTaO_3$, and $CdS/Pt/NaTaO_3$; (b) ΔG_{H^*} of $NaTaO_3$, $CdS/NaTaO_3$ and $CdS/Pt/NaTaO_3$; (c) Structural model diagram of the adsorption site structure and (d) H_2 adsorption free energy change of $CdS/Pt/NaTaO_3$ heterojunction during the whole process of splitting water into hydrogen; ISI-XPS of Cd 3d (e), S 2p (f) and Ta 4f (g) for 25 %CdS/2 %Pt/$NaTaO_3$; (h) Schematic *Z*-scheme mechanism of photogenerated carriers separation and transfer process of $CdS/Pt/NaTaO_3$.

electron conduction properties in $CdS/Pt/NaTaO_3$ heterojunction, enabling electrons to be rapidly conducted from $NaTaO_3$ to CdS via Pt, thereby participating in photocatalytic hydrogen production reactions. This process has the lowest reaction barrier. Moreover, the Gibbs free energy changes of the ternary $CdS/Pt/NaTaO_3$ heterojunction in the full pathway of water splitting have been computationally analyzed (Fig. 10c-d), and the results show a well-defined H_2 evolution of the $CdS/Pt/NaTaO_3$ heterojunction from H_2O to HO-H to H*.

In situ light irradiated X-ray photoelectron spectroscopy (ISI-XPS) (Fig. 10e-g) was used to analyze the electron migration direction in the heterojunction before and after illumination. After illumination, the binding energies of Cd and S in CdS shifted to lower values, whereas that of Ta increased. This result implies that photogenerated electrons from $NaTaO_3$ in $CdS/Pt/NaTaO_3$ transfer to CdS upon illumination, providing compelling evidence for the existence of the Z-scheme heterojunction. Experimental and theoretical evidence demonstrate that Pt NPs act as electron mediators in the $CdS/Pt/NaTaO_3$ ternary system, bridging CdS QDs and $NaTaO_3$ MCs to form a unique heterojunction structure. Based on the band structures of $NaTaO_3$ and CdS, we propose a Z-scheme mechanism for photocatalytic H_2 evolution in this ternary composite material (Fig. 10h) [43–45]. Under the light irradiation condition, the electrons on the VB of $NaTaO_3$ MCs and CdS QDs were excited to the CB, leaving the photogenerated holes in the relevant VB positions. At this time, the Fermi energy level is balanced at the interface formed by $NaTaO_3$ MCs, Pt NPs, and CdS QDs. Because of the excellent electron transfer capability of Pt NPs, the electrons in the CB of $NaTaO_3$ can easily be transferred to Pt NPs through the Schottky barrier, and then transferred from the surface of the Pt NPs to the VB of the CdS and rapidly combine with the photogenerated holes of CdS. Due to the effective transport and recombination of photogenerated electrons and holes in the internal pathways mentioned above, effective electrons are retained in the CB of the CdS QDs, which can be sufficiently contacted with the H^+ in water to trigger the reduction reaction to produce H_2. In addition, the holes left in the VB of $NaTaO_3$ are eliminated by oxidation reaction with the sacrificial agent lactic acid. Therefore, strong oxidation holes are retained on the $NaTaO_3$, and strong reduction electrons are retained on the CdS QDs, which effectively inhibits the combination of photogenerated electron holes. Through this process, the whole electron migration route was greatly shortened, and efficient photocatalytic hydrogen production reaction activity was achieved.

4. Conclusion

In conclusion, a novel all-solid-state close-contact *Z*-scheme heterojunction $CdS/Pt/NaTaO_3$ was prepared using hydrothermal, in situ photodeposition, and solvothermal methods. The hydrogen production performance of $CdS/Pt/NaTaO_3$ is significantly improved to 19,844 $\mu mol \cdot g^{-1} \cdot h^{-1}$, which is 325 times higher than that of the pure-phase $NaTaO_3$ MCs and 15 times higher than that of the pure-phase CdS QDs, respectively. It is demonstrated by experimental and computational results that the Pt NPs are located at the heterojunction interface between $NaTaO_3$ and CdS QDs, which firmly connect $NaTaO_3$ and CdS QDs to form a ternary composite heterojunction structure in a bridge-like manner. Pt acts as an electron conductor, allowing electrons to migrate from $NaTaO_3$ to CdS via Pt. This unique structure effectively overcomes the inherent drawbacks of $NaTaO_3$ and CdS. On one hand, the construction of the heterojunction synergistically modulates the energy band structure of the system, enhancing visible light absorption and mitigating the limitation posed by the wide bandgap of $NaTaO_3$. On the other hand, the Pt-bridged *Z*-scheme charge transfer pathway not only significantly promotes the spatial separation of photogenerated electron-hole pairs and suppresses their recombination. More crucially,

this mechanism directs and confines the strongly oxidative holes in the VB of $NaTaO_3$, thereby markedly alleviating the photocorrosion issue of CdS. Ultimately, these combined effects lead to a remarkable enhancement in both the activity and stability of photocatalytic H_2 evolution. Moreover, the CdS/Pt/$NaTaO_3$ heterojunction exhibits the lowest overpotential and possesses the lowest reaction barrier during photocatalytic water splitting for H_2 production, thus favoring H_2 generation. This work provides a new idea for the application of a novel $NaTaO_3$-based heterojunction system in photocatalysis. Beyond the specific CdS/Pt/$NaTaO_3$ system, the bridging strategy demonstrated herein offers a universal design principle for constructing efficient all-solid-state Z-scheme heterojunctions. This approach is readily adaptable to other combinations of wide-bandgap (e.g., TiO_2, $BiVO_4$) and narrow-bandgap semiconductors (e.g., g-C_3N_4, $CuInS_2$), where a central mediator can orchestrate directional charge flow. Future endeavours shall concentrate on investigating cost-effective substitutes for Pt, such as non-precious metal materials (e.g., Ni NPs, Cu NPs) or conductive carbon materials, to advance the practical and scalable application of this photocatalytic systerm.

CRediT authorship contribution statement

Jiayi Meng: Writing – original draft, Validation, Investigation. **Juhua Zhang:** Methodology, Conceptualization. **Yamei Huang:** Formal analysis. **Zizheng Wang:** Investigation. **Yifan Liao:** Writing – review & editing. **Quanmei Zhou:** Validation. **Yuchen Wei:** Formal analysis. **Linlin Gao:** Data curation. **Wei-Lin Dai:** Writing – review & editing, Visualization, Supervision, Project administration, Funding acquisition.

Declaration of competing interest

The authors declare that they have no known competing financial interests or personal relationships that could have appeared to influence the work reported in this paper.

Acknowledgments

This work was funded by the National Key Research and Development Program of China (2021YFA1501404), Natural Science Foundation of Shanghai (22ZR1404200), and the Science and Technology Commission of Shanghai Municipality (2024ZDSYS02).

Appendix A. Supplementary data

Supplementary data to this article can be found online at https://doi.org/10.1016/j.cej.2025.170413.

Data availability

Data will be made available on request.

References

[1] S. Zhang, Z. Zhang, Y. Si, B. Li, F. Deng, L. Yang, X. Liu, W. Dai, S. Luo, Gradient hydrogen migration modulated with self-adapting S vacancy in copper-doped $ZnIn_2S_4$ nanosheet for photocatalytic hydrogen evolution, ACS Nano 15 (2021) 15238–15248, https://doi.org/10.1021/acsnano.1c05834.

[2] Z. Wang, X. Huang, Y. Jia, L. Guo, H. Wang, W. Dai, Localized surface plasmon resonance-induced bidirectional electron transfer of formic acid adsorption for boosting photocatalytic hydrogen production on Ni/TiO_2, Chem. Eng. J. 482 (2024) 148942, https://doi.org/10.1016/j.cej.2024.148942.

[3] X. Shi, C. Dai, X. Wang, J. Hu, J. Zhang, L. Zheng, L. Mao, H. Zheng, M. Zhu, Protruding Pt single-sites on hexagonal $ZnIn_2S_4$ to accelerate photocatalytic hydrogen evolution, Nat. Commun. 13 (2022) 1287, https://doi.org/10.1038/s41467-022-28995-1.

[4] H. Zhang, Y. Huang, X. Wang, J. Meng, L. Gao, Y. Li, Y. Zhang, W.-L. Dai, Tightly-bound interfaces between $ZnIn_2S_4$ nanosheets and few-layered Mo_2TiC_2 MXene induced highly efficient noble-metal-free Schottky junction for photocatalytic hydrogen evolution, Sep. Purif. Technol. 360 (2024) 131199, https://doi.org/10.1016/j.seppur.2024.131199.

[5] G. Liu, Y. Zhang, L. Xu, B. Xu, F. Li, A PW_{12}/Bi_2WO_6 composite photocatalyst for enhanced visible light photocatalytic degradation of organic dye pollutants, New J. Chem. 8 (2019) 3469–3475, https://doi.org/10.1039/c8nj05862h.

[6] L. Zhang, C. Yang, K. Lv, Y. Lu, Q. Li, X. Wu, Y. Li, X. Li, J. Fan, M. Li, SPR effect of bismuth enhanced visible photoreactivity of Bi_2WO_6 for NO abatement, Chin. J. Catal. 5 (2019) 755–764, https://doi.org/10.1016/s1872-2067(19)63320-6.

[7] K. Huang, G. Liang, S. Sun, H. Hu, X. Peng, R. Shen, X. Li, Interface-induced charge transfer pathway switching of a Cu_2O-TiO_2 photocatalyst from p-n to S-scheme heterojunction for effective photocatalytic H_2 evolution, J. Mater. Sci. Technol. 193 (2024) 98–106, https://doi.org/10.1016/j.jmst.2024.01.034.

[8] M. Lv, X. Sun, S. Wei, C. Shen, Y. Mi, X. Xu, Ultrathin lanthanum tantalate perovskite nanosheets modified by nitrogen doping for efficient photocatalytic water splitting, ACS Nano 11 (2017) 11441–11448, https://doi.org/10.1021/acsnano.7b06131.

[9] J. Hou, S. Cao, Y. Wu, F. Liang, L. Ye, Z. Lin, L. Sun, Perovskite-based nanocubes with simultaneously improved visible-light absorption and charge separation enabling efficient photocatalytic CO_2 reduction, Nano Energy 30 (2016) 59–68, https://doi.org/10.1016/j.nanoen.2016.09.033.

[10] A.S. Basaleh, A. Shawky, Z.I. Zaki, Visible light-driven photodegradation of ciprofloxacin over sol-gel prepared Bi_2O_3-modified La-doped $NaTaO_3$ nanostructures, Ceram. Int. 47 (2021) 19205–19212, https://doi.org/10.1016/j.ceramint.2021.03.268.

[11] A.P. Singh, S. Kumar, M. Thirumal, Efficient charge transfer in heterostructures of CdS/$NaTaO_3$ with improved visible-light-driven photocatalytic activity, ACS Omega 4 (2019) 12175–12185, https://doi.org/10.1021/acsomega.9b01133.

[12] F.-F. Li, D.-R. Liu, G.-M. Gao, B. Xue, Y.-S. Jiang, Improved visible-light photocatalytic activity of $NaTaO_3$ with perovskite-like structure via sulfur anion doping, Appl. Catal. B Environ. Energy 166-167 (2015) 104–111, https://doi.org/10.1016/j.apcatb.2014.10.049.

[13] Z. Sun, W. Lv, Y. Song, X. Zeng, Z. Fu, Treatment of xanthate flotation reagent wastewater with La/$NaTaO_3$ composite photocatalyst: synthesis, degradation and mechanism study, Mater. Sci. Semicond. Process. 190 (2025) 109300, https://doi.org/10.1016/j.mssp.2025.109300.

[14] L. Bi, R. Zhang, K. Zhang, Y. Lin, D. Wang, X. Zou, T. Xie, Sulfidization of platinum nickel bimetal-decorated g-C_3N_4 for photocatalytic hydrogen production: photogenerated charge behavior study, ACS Sustain. Chem. Eng. 7 (2019) 15137–15145, https://doi.org/10.1021/acssuschemeng.9b04153.

[15] P.A. Pepin, J.D. Lee, A.C. Foucher, C.B. Murray, E.A. Stach, J.M. Vohs, The influence of surface platinum deposits on the photocatalytic activity of anatase TiO_2 nanocrystals, J. Phys. Chem. C 123 (2019) 10477–10486, https://doi.org/10.1021/acs.jpcc.9b01861.

[16] C. Dong, C. Lian, S. Hu, Z. Deng, J. Gong, M. Li, H. Liu, M. Xing, J. Zhang, Size-dependent activity and selectivity of carbon dioxide photocatalytic reduction over platinum nanoparticles, Nat. Commun. 9 (2018) 1252, https://doi.org/10.1038/s41467-018-03666-2.

[17] Z. Zhang, Y. Kang, L.-C. Yin, P. Niu, C. Zhen, R. Chen, X. Kang, F. Wu, G. Liu, Constructing CdSe QDs modified porous g-C_3N_4 heterostructures for visible light photocatalytic hydrogen production, J. Mater. Sci. Technol. 95 (2021) 167–171, https://doi.org/10.1016/j.jmst.2021.02.068.

[18] X. Yang, J. Ma, T. Wang, B. Wang, D. Meng, Y. Wang, Synthesis, growth mechanism and photocatalytic property of CdS with different kinds of surfactants, New J. Chem. 43 (2019) 10126–10133, https://doi.org/10.1039/c9nj01856e.

[19] Z. Chen, H. Gong, Q. Liu, M. Song, C. Huang, $NiSe_2$ nanoparticles grown in situ on CdS nanorods for enhanced photocatalytic hydrogen evolution, ACS Sustain. Chem. Eng. 19 (2019) 16720–16728, https://doi.org/10.1021/acssuschemeng.9b04173.

[20] J. Kundu, B.K. Satpathy, D. Pradhan, Composition-controlled CdS/ZnS heterostructure nanocomposites for efficient visible light photocatalytic hydrogen generation, Ind. Eng. Chem. Res. 58 (2019) 22709–22717, https://doi.org/10.1021/acs.iecr.9b03764.

[21] T.Y. Huang, Z. Yang, S.Y. Yang, Z.H. Dai, Y.J. Liu, J.H. Liao, G.Y. Zhong, Z.J. Xie, Y. P. Fang, S.S. Zhang, Construction of 2D/2D $Ti_3C_2T_x$ MXene/CdS heterojunction with photothermal effect for efficient photocatalytic hydrogen production, J. Mater. Sci. Technol. 171 (2024) 1–9, https://doi.org/10.1016/j.jmst.2023.07.010.

[22] Y.-H. Cui, L.-J. Tian, W.-W. Li, W.-K. Wang, W. Wei, P.K.S. Lam, L.-H. Zhang, P. Zhou, H.-Q. Yu, Solar-energy-facilitated CdS_xSe_{1-x} quantum dot bio-assembly in Escherichia coli and Tetrahymena pyriformis, J. Mater. Chem. 7 (2019) 6205–6212, https://doi.org/10.1039/c9ta00822e.

[23] L.C. Spangler, J.P. Cline, J.D. Sakizadeh, C.J. Kiely, S. McIntosh, Enzymatic synthesis of supported CdS quantum dot/reduced graphene oxide photocatalysts, Green Chem. 21 (2019) 4046–4054, https://doi.org/10.1039/c9gc00097f.

[24] Y. Du, L. Li, Y. Tang, J. Li, Q. Guo, G. Yue, Effective degradation of multiple antibiotics by 0D/3D/2D dual Z-heterojunction photocatalyst CdS QDs/Bi_2WO_6/g-C_3N_4 and study of degradation mechanism, Appl. Surf. Sci. 697 (2025) 163004, https://doi.org/10.1016/j.apsusc.2025.163004.

[25] T. Zhang, W. Wang, X. Jiang, H. Wang, Z.-H. He, Y. Yang, K. Wang, Z.-T. Liu, B. Han, Fabricating CdS/Ag/$BiVO_4$ Z-heterojunction for solvent-free photocatalytic oxidation of amines, Green Chem. 26 (2024) 3338–3345, https://doi.org/10.1039/d3gc04644c.

[26] F. Wang, S. Zhang, W. Jing, H. Qiu, Y. Liu, L. Guo, Double Z-scheme in SnO_2/SnS_2/Cu_2SnS_3 heterojunction for photocatalytic reduction of CO_2 to ethanol, J. Mater. Sci. Technol. 189 (2024) 146–154, https://doi.org/10.1016/j.jmst.2024.01.002.

[27] L. Hua, Y. Wang, Z. Li, Arsenene/Ti_2CO_2 heterojunction as a promising Z-scheme photocatalyst for overall water splitting, Adv. Funct. Mater. 34 (2024) 2408353, https://doi.org/10.1002/adfm.202408353.

[28] M.-J. Ran, M. Wang, Z.-Y. Hu, Y.-F. Huang, L.-D. Wang, L. Wu, M.-M. Yuan, J. Zhang, B. Li, G. Van Tendeloo, Y. Li, B.-L. Su, A hollow core-shell $TiO_2/NiCo_2S_4$ Z-scheme heterojunction photocatalyst for efficient hydrogen evolution, J. Mater. Sci. Technol. 212 (2025) 182–191, https://doi.org/10.1016/j.jmst.2024.06.016.
[29] M. Shi, X. Wu, Y. Zhao, R. Li, C. Li, Unlocking the key to photocatalytic hydrogen production using electronic mediators for Z-scheme water splitting, J. Am. Chem. Soc. 147 (2025) 3641–3649, https://doi.org/10.1021/jacs.4c15540.
[30] L. Zuo, N. Yang, W. Xia, X. Zeng, R. Cao, Z-scheme NiS@ZnCdS heterostructures and their boosted photocatalytic H_2 evolution, Appl. Surf. Sci. 689 (2025) 162447, https://doi.org/10.1016/j.apsusc.2025.162447.
[31] L. Wang, H. Xiao, L. Yang, J. Li, J. Zi, Z. Lian, Hollow nanobox-shaped $Cu_{2-x}S@Zn_xCd_{1-x}S$ heterojunction by light multireflection with Z-scheme mechanism for enhanced photocatalytic hydrogen production, Adv. Funct. Mater. 35 (2025) 2416358, https://doi.org/10.1002/adfm.202416358.
[32] C. Jiang, Y. Qiu, X. Xin, Y. Li, H. Li, H. Wang, J. Xu, H. Lin, L. Wang, V. Turkevych, MOF-templated tubular $Ni_{1-x}Co_xS_2$-CdS heterojunction with intensified direct Z-scheme charge transmission for highly promoted visible-light photocatalysis, Nano Res 17 (2024) 6281–6293, https://doi.org/10.1007/s12274-024-6636-z.
[33] L. Cheng, Y. Li, A. Chen, Y. Zhu, C. Li, Impacts on carbon dioxide electroreduction of cadmium sulfides via continuous surface sulfur vacancy engineering, Chem. Commun. 56 (2020) 563–566, https://doi.org/10.1039/c9cc08330h.
[34] J. Shi, S. Feng, T. Chen, Z. Liu, X. Yue, High-efficiency visible light photocatalytic performances of the CdS(HS)/g-C_3N_4 composites: the role of intimate connection and hollow structure, J. Mater. Sci. Mater. Electron. 30 (2019) 10867–10878, https://doi.org/10.1007/s10854-019-01430-w.
[35] L. Tang, C. Feng, Y. Deng, G. Zeng, J. Wang, Y. Liu, H. Feng, J. Wang, Enhanced photocatalytic activity of ternary Ag/g-C_3N_4/$NaTaO_3$ photocatalysts under wide spectrum light radiation: the high potential band protection mechanism, Appl. Catal. B Environ. Energy 230 (2018) 102–114, https://doi.org/10.1016/j.apcatb.2018.02.031.
[36] K.H. Reddy, S. Martha, K.M. Parida, Facile fabrication of Bi_2O_3/Bi–$NaTaO_3$ photocatalysts for hydrogen generation under visible light irradiation, RSC Adv. 2 (2012) 9423–9436, https://doi.org/10.1039/c2ra21083e.
[37] V. Shanker, S.L. Samal, G.K. Pradhan, C. Narayana, A.K. Ganguli, Nanocrystalline $NaNbO_3$ and $NaTaO_3$: Rietveld studies, Raman spectroscopy and dielectric properties, Solid State Sci. 11 (2009) 562–569, https://doi.org/10.1016/j.solidstatesciences.2008.08.001.
[38] P.V. Braun, S.I. Stupp, CdS mineralization of hexagonal, lamellar, and cubic lyotropic liquid crystals, Mater. Res. Bull. 34 (1999) 463–469, https://doi.org/10.1016/s0025-5408(99)00030-6.
[39] K. Murakoshi, H. Hosokawa, M. Saitoh, Y. Wada, T. Sakata, H. Mori, M. Satoh, S. Yanagida, Preparation of size-controlled hexagonal CdS nanocrystallites and the characteristics of their surface structures, J. Chem. Soc. Faraday Trans. 94 (1998) 579–586, https://doi.org/10.1039/a707192b.
[40] W. Vogel, L. Timperman, N. Alonso-Vante, Probing metal substrate interaction of Pt nanoparticles: structural XRD analysis and oxygen reduction reaction, Appl. Catal., A 377 (2010) 167–173, https://doi.org/10.1016/j.apcata.2010.01.034.
[41] Q. Liu, Y. Chai, L. Zhang, J. Ren, W.-L. Dai, Highly efficient Pt/$NaNbO_3$ nanowire photocatalyst: its morphology effect and application in water purification and H_2 production, Appl. Catal. B Environ. Energy 205 (2017) 505–513, https://doi.org/10.1016/j.apcatb.2016.12.065.
[42] H. Li, X. Shi, X. Liu, X. Li, Synthesis of novel, visible-light driven S,N-doped $NaTaO_3$ catalysts with high photocatalytic activity, Appl. Surf. Sci. 508 (2020) 145306, https://doi.org/10.1016/j.apsusc.2020.145306.
[43] F. Wang, N. Ma, L. Zheng, L. Zhang, Z. Bian, H. Wang, Interface engineering of p-p Z-scheme BiOBr/$Bi_{12}O_{17}Br_2$ for sulfamethoxazole photocatalytic degradation, Chemosphere 307 (2022) 135666, https://doi.org/10.1016/j.chemosphere.2022.135666.
[44] G. Liao, C. Li, S.-Y. Liu, B. Fang, H. Yang, Emerging frontiers of Z-scheme photocatalytic systems, Trends Chem. 4 (2022) 111–127, https://doi.org/10.1016/j.trechm.2021.11.005.
[45] J. Li, H. Yuan, W. Zhang, B. Jin, Q. Feng, J. Huang, Z. Jiao, Advances in Z-scheme semiconductor photocatalysts for the photoelectrochemical applications: a review, Carbon Energy 4 (2022) 294–331, https://doi.org/10.1002/cey2.179.